Rigid-body fitting to atomic force microscopy images for inferring probe shape and biomolecular structure

Short title: Inferring probe shape and molecular structure from AFM images

Toru Niina[1], Yasuhiro Matsunaga[2], and Shoji Takada[1*]

[1] Department of Biophysics, Graduate School of Science, Kyoto University, Kyoto 606-8502, Japan.

[2] Graduate School of Science and Engineering, Saitama University, Shimo-Okubo 255, Sakura, Saitama 338-8570, Japan.

*Corresponding author.

Keywords: high-speed atomic force microscopy, exhaustive search, probe tip radius, afmize

Abstract

High-speed (HS) atomic force microscopy (AFM) can visualize real-time dynamics of functional biomolecules near the physiological condition, but the observed data are limited to the surface height of specimens. Since the HS-AFM images highly depend on the probe tip shape, for successful inference of molecular structures from the measurement, the knowledge of the probe shape is required, but is often missing. Here, we developed a method of the rigid-body fitting to HS-AFM images, which simultaneously finds the shape of the probe tip and the placement of the molecular structure via an exhaustive search. We examined four similarity scores via twin-experiments for four test proteins: Of the four scores, the cosine similarity generally worked best, whereas the pixel-RMSD was also useful especially for the placement of small proteins. We then applied the method to two experimental HS-AFM images inferring the probe shape and the molecular placement. The inferred tip shape and placement results can be further refined by other methods, such as the flexible fitting molecular dynamics simulations. The developed software is publicly available.

Author Summary

Observation of functional dynamics of individual biomolecules is important to understand molecular mechanisms of cellular phenomena. High-speed (HS) atomic force microscopy (AFM) is a powerful tool that enables us to visualize the real-time dynamics of working biomolecules under near-physiological conditions. However, the information available by the HS-AFM images is limited to the two-dimensional surface shape detected via the force to the probe. While the surface information is affected by the shape of the probe tip, the probe shape itself cannot be directly measured before each HS-AFM measurement. To overcome this problem, we have developed a computational method to simultaneously infer the probe tip shape and the molecular placement from an HS-AFM image. We show that our method successfully estimates the effective HS-AFM tip shape and visualizes a structure with a more accurate placement. The estimation of a molecular placement with the correct probe tip shape enables us to obtain more insights into functional dynamics of the molecule from HS-AFM images.

Introduction

Virtually all the cellular phenomena are accomplished by functional dynamics of individual biomolecules, and thus observation of their movements at the single-molecule level is a key step to understand molecular mechanisms. Among many single-molecular observation techniques(1) such as fluorescence resonance energy transfer microscopies(2–4), single particle tracking(5), optical tweezers(6), and atomic force microscopies (AFM)(7), the high-speed AFM (HS-AFM) is unique in that it can observe real-time structural dynamics of biomolecules at work near the physiological condition(8,9). The HS-AFM has been extensively used in biophysics to successfully observe structural dynamics of molecular motors(10–12), large biomolecular complexes(13,14), intrinsically disordered proteins(15), and so on. Thanks to recent developments, the frame acquisition rate of the HS-AFM reaches tens of frames per second, keeping its high spatial resolution, ~2 nm in lateral direction and ~0.15 nm in vertical direction to the stage(9).

Although the HS-AFM is powerful, it remains difficult to estimate three-dimensional molecular structure directly from the HS-AFM image. This is in part because the AFM is a scanning force microscopy and thus the AFM measurement is limited to the two-dimensional surface height information detected via the force to the probe. Moreover, to transform the AFM data into three-dimensional structural information, one needs to know the probe tip shape, which is normally unknown *a priori*. While there are several works that estimate the orientation and location of a molecule from an AFM image(16–20), only a few can estimate the shape of the tip used in the experiments, most of which estimate only the tip radius. Trinh and colleagues(21) developed a method to estimate the probe tip radius by using tobacco mosaic virus (TMV) as a calibrator and proposed to always observe it with the samples of interest. Although TMV is a stable and easy-to-use calibrator, still it is not always easy to observe it at the same condition as other molecules that generally requires different conditions to be stabilized on the AFM stage. Also, a recent work(22) that reconstructs the three-dimensional structures of amyloid fibril developing a method to refine the topography carefully estimates the probe tip radius. However, they use the ideal corkscrew symmetry in the specimen and it is not always applicable to other biomolecules. In general, the probe tip shape varies sample by sample. Its radius is typically sharpened to ~5 nm and sometimes less than 1 nm, and it is almost impossible to observe the shape of the probe tip at such a high resolution before using it in the experiment(8). Recently, we developed a computational method(23) that enables to reconstruct a molecular model from an AFM image taking the conformational change into account, inspired by the flexible fitting method for cryo-electron microscopy (cryo-EM) electron density map(24). We also showed that, from the result of the flexible fitting, we can estimate the effective tip radius(25). However, the biased molecular dynamics is rather time−consuming method that requires large computational resources. Thus, it is not yet useful enough to estimate the tip probe. Also, the information that can be reconstructed from the flexible fitting is limited to the parameter used in the biasing potential and sometimes it might be hard to interpret as the physical shape of the probe.

In this paper, we developed a rigid-body fitting method to simultaneously search the probe tip shape and the structure placement best-fit to a given AFM image. The tip shape can be estimated from the optimization of the similarity between an experimental AFM image and pseudo-AFM image generated from a molecular model with a varying geometry of the probe tip, as in our previous approach(25). In contrast to

the previous approach, our current method directly models the physical shape of the probe tip, and thus is more straightforward to interpret the estimation results. First, by twin experiments, we examined four different image similarity scores for three monomeric proteins and investigated the relationships between the size of proteins, the image similarity scores, and the accuracy of tip shape inference. Next, we performed a twin experiment using a model of actin filament and confirmed that our method works well even when the template structure fits only to a part of an observed AFM image. Finally, we applied our method to two real experimental HS-AFM images, the actin filament and the oligomeric $FlhA_C$, and estimated the probe shape in the experimental measurements.

Methods

Collision-detection Method for Pseudo-AFM Image Generation

We utilized the conventional collision-detection method to generate pseudo-AFM images from a structural model of the target molecule(23,26–28). The method calculates the height at which the probe hits an atom in the target molecules tethered on the stage. The stage surface is set to the *XY*-plane, on which the molecules are placed to the positive *Z* side. We approximate the probe tip as a hemisphere (the radius 0.5 to 5.0 nm) combined with a circular frustum of a cone (the half-apex angle 5 to 30 degree), with its symmetric axis parallel to *Z*-axis (Fig 1A). For each pixel, the probe center is fixed to the *XY*-coordinates of the center of the pixel. Moving down the probe from the top, the method detects the collision between the probe tip and atoms in the target. In the twin-experiments, when we make a reference AFM image that serves as an "experimental AFM image", after determining the collision heights of all the pixels, we added spatially independent Gaussian noise with the mean 0 nm and the standard deviation 0.3 nm, which is a typical level of noise as is shown in Results.

Fig 1. A pseudo-AFM image generation scheme and the search algorithm. (A) The AFM probe tip (grey) is modeled as a hemisphere connected to a circular frustum of a cone. The shape of tip is determined by the tip radius (r) and a half-apex angle of cone (θ). The pseudo-AFM image represents the height of the tip when the tip collides with any atom (red circle) of the target molecule. (B) The exhaustive search finds the best match in the discrete space made of the orientation and the translation of the target molecule and the radius and the half-apex angle of the probe tip.

Image Similarity Calculation

To calculate similarity between a pseudo-AFM image generated from a molecular model and the reference image (the AFM experimental data in normal use and a generated image in the case of twin-experiments), we examined four different similarity score functions; the cosine similarity, the correlation coefficient, the pixel-RMSD, and the penalty function. Through twin-experiments, we compared their performances.

Since the experimental/reference AFM image contains non-negligible noise, the search method may tend to place the molecule at a high-noise spot as an artifact. To reduce this unfavorable case, we limited the

pixels used to calculated the similarity functions. In the similarity calculation, we trimmed both pseudo- and reference AFM images by the minimum bounding rectangle of non-zero-height pixels in the pseudo-AFM image. We note that, due to the probe tip size, the pseudo-AFM image can have non-zero height even at the pixel where the molecule is absent. This is especially significant when the target molecule is tall, the probe tip radius is large, and the probe apex angle is large.

Cosine Similarity

The cosine similarity is the function used in our previous research of flexible fitting method(23), though it was called a "modified correlation coefficient" previously, and also used in the field of cryo-EM flexible fitting(24). The form of the function resembles to the correlation coefficient, but each term does not subtract the mean values. Thus, unlike the correlation coefficient, the cosine similarity depends not only on the relative height of pixels, but also the absolute height of pixels.

$$c.s.\left(H^{(sim)};H^{(ref)}\right)=\frac{\sum_p^{pixel} H_p^{(sim)} H_p^{(ref)}}{\sqrt{\sum_p^{pixel}\left(H_p^{(sim)}\right)^2}\sqrt{\sum_p^{pixel}\left(H_p^{(ref)}\right)^2}}$$

Here, $H^{(sim)}$ denotes the pseudo-AFM image generated from a molecular model and $H^{(ref)}$ denotes the reference AFM image. H_p denotes the height at the pixel p. The cosine similarity takes 1.0 if two images are identical, and -1.0 if images are totally opposite. To use this function in a minimization protocol, we defined the corresponding cost function as follows.

$$V_{c.s.}\left(H^{(\mathrm{sim})};H^{(ref)}\right)=1.0-c.s.\left(H^{(\mathrm{sim})};H^{(\mathrm{ref})}\right)$$

Correlation Coefficient

The correlation coefficient is a well-known measure that represents how two data sets resemble each other.

$$c.c.\left(H^{(sim)};H^{(ref)}\right)=\frac{\sum_p^{pixel}\left(H_p^{(sim)}-\langle H^{(sim)}\rangle\right)\left(H_p^{(ref)}-\langle H^{(ref)}\rangle\right)}{\sqrt{\sum_p^{pixel}\left(H_p^{(sim)}-\langle H^{(sim)}\rangle\right)^2}\sqrt{\sum_p^{pixel}\left(H_p^{(ref)}-\langle H^{(ref)}\rangle\right)^2}}$$

Since each term subtracts its mean value, it does not depend on the absolute height. Similar to the cosine similarity, it takes 1.0 if the two images are identical and -1.0 if images are completely opposite. To use this in the minimization, we also defined the cost function below.

$$V_{c.c.}\left(H^{(\mathrm{sim})};H^{(ref)}\right)=1.0-c.c.\left(H^{(\mathrm{sim})};H^{(\mathrm{ref})}\right)$$

Here, $\langle x\rangle$ denotes the mean value of x's.

pixel-RMSD

The root mean square displacement (RMSD) is a widely used measure to calculate the difference between two data. Here we utilized the RMSD of pixel heights as the cost function between the two images. To distinguish it from the RMSD between two structural models, we call it the pixel-RMSD hereafter. The RMSD takes 0 if the two images are identical and takes a positive value if the two images are different. We used the pixel-RMSD value itself as the cost function in the minimization.

$$V_{pixel-RMSD}\left(H^{(sim)};H^{(ref)}\right) = \sqrt{\frac{1}{N}\sum_{p}^{\text{pixel}}\left(H_p^{(\text{sim})} - H_p^{(\text{ref})}\right)^2}$$

where N means the number of pixels.

Penalty function

In a previous related study, a rigid body fitting method to an AFM image using molecular docking algorithms was examined(18,19). That study utilized an existing docking method, it has an advantage in terms of efficiency but, since it does not have any model of the probe, it cannot be used to reconstruct probe shape. Here, inspired by this previous approach, we define a penalty function, somewhat resemble to, but not identical to, the previous one. If a height at a pixel in a pseudo-AFM image exceeds the height of the corresponding pixel in the reference image, the cost increases. If a height of a pixel in a pseudo-AFM image is less than and close to that of the corresponding pixel in the reference image, the cost decreases. Otherwise, the cost does not change. Specifically, we define the penalty function as follows:

$$V_{penalty}\left(H^{(sim)};H^{(ref)}\right) = \sum_{p}^{pixel} Penalty\left(H_p^{(sim)};H_p^{(ref)}\right)$$

$$Penalty\left(H^{(sim)};H^{(ref)}\right) = \begin{cases} k_{penalty} & \cdots & \left(H^{(ref)} < H^{(sim)}\right) \\ -k_{reward} & \cdots & \left(H^{(ref)} < H^{(sim)} + thickness\right) \\ 0 & \cdots & otherwise \end{cases}$$

In this work, we chose 1.2 nm as the thickness of the favorable region, the same value in the previous work, 10.0 as the $k_{penalty}$ and 1.0 as the k_{reward}. Note that this penalty function is not exactly the same as that of the previous research. Since our purpose is to reconstruct the probe shape as well as the three-dimensional structural model, we need to use a pseudo-AFM image generated with a probe model. Thus, we used heights of the pixels, not the height of the atoms in a model.

Exhaustive Search Rigid-body Fitting Method

In this work, we exhaustively searched the discretized orientation and translation of a molecule as well as the discretized radius and the half-apex angle of the probe tip to find the optimal combination of the molecular

placement and the probe shape that generates the pseudo-AFM image with the highest similarity to the reference AFM image.

To search the orientation of a molecule, we first define a step size of the rotational angle that divides 360 degree into a multiple of 4. Unless otherwise noted, we use 10 degree as the step size. Then we distribute points on a spherical surface evenly, according to the step size (Fig 1B). To distribute evenly spaced points on the spherical surface, we divided the great circle by the step size starting from the pole where the positive side of Z-axis intersects the spherical surface. Since we chose the step size to make the number of dividing points a multiple of 4, we have a point on the equator where the XY-plane intersects the spherical surface. When we call the point at the pole as the 0-th point, the 9-th point is on the equator. For each point, the n-th point, chosen on the great circle, we consider the surface that passes through the point and that is perpendicular to the Z-axis. We then divide the section of the spherical surface and the n-th plane, i.e., the n-th circle, into n components. In this manner, we can distribute points on spherical surface almost evenly. Finally, we rotate the molecule to make Z-axis turns to those points, and then rotate the molecule around the new Z-axis.

For each orientation, we first generate the pseudo-AFM image and calculate the bounding rectangle of non-zero-height pixels. We then move the image translationally in XY-direction in the range where the bounding rectangle does not stick out of the reference AFM image. Here, we define the step size of the translation along the X- and Y-axis as the pixel size. We search the location of molecule along Z-axis only if the reference image contains a pixel that is higher than any of the pixel in pseudo-AFM image. Since the resolution of HS-AFM image in Z-axis is typically from 0.05 nm to 0.15 nm, we used 0.064 nm as the step size along the Z-axis.

Twin Experiment

To assess the performance of the methods and compare the four similarity score functions unambiguously, we first conduct the so-called twin-experiments. A twin-experiment begins with a random choice of a position and an orientation of a target protein structure bound on a surface (see the next subsection for more details). We also choose a probe tip radius and the half-apex angle. These together serve as the ground-truth data of the molecular placement and the probe shape. Using this ground-truth setup, we generate an AFM image via the collision-detection method, to which we added 10 different realizations of Gaussian noises. The generated 10 AFM images play the role of "experimental AFM images" and are referred as the reference AFM images. Then, applying the exhaustive search rigid-body fitting method to the reference AFM image, we seek the lowest-scored placement and the probe shape.

The deviation between the ground-truth structure and the best-fit placement found in the exhaustive search is measured as the RMSD. For this purpose, we simply calculated the structure RMSD without further optimizing the alignment. To distinguish it from the pixel-RMSD used to measure the difference of two AFM images, we will call it as the structure-RMSD hereafter. Note that, since the orientation search uses relatively large step size (10 degree), the best orientation may still have non-negligible structure-RMSD.

Protein Modeling

In this paper, we used dynein(29), myosin [pdb id: 2KIN](30), actin monomer, and actin filament [pdb id: 6BNO](31) as the targets of twin experiments. To remove the heterogeneity in the actin filament structure, we aligned the chain A in the PDB structure to the other chains and replaced them by the chain A structure. Then we aligned the last monomer of the octamer by the first monomer and obtained 15-mer and 29-mer structures of actin filament.

In the HS-AFM experimental setup, normally proteins are weakly bound to the stage to moderate the fast Brownian diffusion. To mimic this situation while generating the reference image in the twin experiments, we calculated an oriented bounding box (OBB) of each protein and rotated the protein to ground the largest face of the OBB on the stage. The OBB axes are calculated based on the principal component analysis of the particle coordinates. The first axis is the first principal component, the second axis is the second principal component rotated to make it perpendicular to the first axis, and the third axis is the cross product of first and second axes. After generating the reference pseudo-AFM images, we rotated the model randomly around X-, Y-, and Z-axis to remove the exact reference structure from the orientation used while searching.

Software availability

The exhaustive search rigid-body fitting method is implemented as a part of software, the afmize(28) . Originally, the afmize was a software to generate a pseudo-AFM image for a given structure, which was developed in our previous work(23). Now, it is extended to perform the rigid-body fitting. The software is freely available for download from https://github.com/ToruNiina/afmize. The method we introduced in this paper is available as the second major release.

Results

Noise analysis in experimental AFM images

Before the setup of twin-experiments, we analyzed several AFM images to estimate the intensity of the noise in the observation. We took two HS-AFM movies that observe $FlhA_C$ monomers(32) and actin filaments because those movies contain large background areas. We selected the last 5 frames of the movies to avoid the transient surge in the noise intensity that occurs when the probe initially approaches to the samples. Then we manually selected background regions from those images and estimated the location of the stage via the standard least square method assuming that the stage is a tilted plane. After that, we collected the deviation of the height of each pixel from the estimated stage position.

Fig S1 shows the histogram of the deviation collected from the experimental observation of $FlhA_C$ monomers and actin filaments. In the case of $FlhA_C$, the histogram fits well to the Gaussian of which the standard deviation is 0.284 nm. In the case of actin filaments, although the distribution slightly deviates from the Gaussian because of some outliers, we fitted it with a Gaussian of which the standard deviation is 0.347 nm. In the observation of actin filament, we recognized several unidentified objects that are much smaller than the filament, which could lead to a small deviation of the stage position and cause the distortion of the

histogram. This is not taken into accounts here. We concluded the noise in the HS-AFM observation can be approximated by the normal distribution with its standard deviation around 0.3 nm. We used this value as a noise level when we generate the reference pseudo-AFM image in the twin experiments.

Twin-experiment: Dynein

As the first test protein, we chose dynein because of its large size and anisotropic shape. Since the random noise in the AFM image is independent from molecules, the larger the target molecule is, the higher signal-to-noise ratio we will obtain. Also, its anisotropic structure is expected to make the orientation search relatively easy.

We placed a dynein model(29) on a surface and generated two reference-AFM images using two different probe shapes, 1 nm / 10 degree (Fig 2A) and 3 nm / 20 degree (Fig 2C) (for the probe shape, the values before and after the slash indicate the tip radius and the half-apex angle, respectively, throughout). These two images are treated as the reference "experimental" AFM images in the context of the twin-experiment. For each reference-AFM image, we applied the exhaustive search method using the four different score functions and compared all the results. Since the probe tip radius used in real HS-AFM imaging(8) is normally between 0.5 nm and 5 nm, we used tip radii of the same range in the search. After obtaining the minimum cost structure, to evaluate the accuracy of the structure placement we calculated the structure-RMSD with respect to the ground-truth structure used to generate the reference AFM image. Note that the exhaustive search method uses the discrete space for the orientation (10 degree here), the translation (same as the pixel size. typically, it is 1 nm), the tip radius (6 values from 0.5 nm to 5.0 nm), and the half-apex angle (10 and 20 degrees). By applying random translation/rotation to prepare the initial structure, we did not include the exactly-correct position/orientation in the test cases. Thus, the minimum possible structure-RMSD may become the same order of sum of the half step sizes.

Fig 2. Twin-experiments for a molecular model of dynein. (A) One of the reference AFM images in the twin-experiment, with the 1 nm / 10 degree probe. (B) The image generated from the predicted structure with the cosine similarity. (C) One of the reference AFM images with the 3 nm / 20 degree probe. (D) The image generated from the predicted structure with the cosine similarity. The color bar shows the height in nm (shared by all of the images here). (E-L) The results of twin-experiment with the reference image generated by the 1 nm / 10 degree probe. Results of 10 replicates are overlaid. The row corresponds to the cost function. The leftmost 4 panels (E, G, I, K) show the lowest scores of images. The next 4 panels (F, H, J, L) show the structure-RMSD of the structures with the lowest score. Red vertical dashed lines show the ground-truth probe shape. (M-T) The results of twin-experiment with the reference image generated by 3 nm / 20 degree probe, shown in the same way as E-L. The cyan vertical dashed lines show the ground-truth probe shape.

Fig 2E-L show the result of the case when the reference-AFM image is generated with the 1 nm / 10 degree probe. When we used the cosine similarity as the cost function, the lowest cost configuration across all the search space was always the one with correct probe shape. The structure-RMSD of those configurations were around 1.3 nm and it is smaller than that of the structures predicted by different probe

shapes (5.6 or 9.8 nm). Contrary, when we used the correlation coefficient, the lowest cost configuration was not the correct probe shape but the probe with 1.0 nm / 20 degree. However, the structure-RMSD of those configurations were almost the same as that of the cosine similarity (~1.3 nm). Thus, it can reconstruct the orientation of molecule even though it cannot accurately infer the probe tip angle. When we used the pixel-RMSD as the cost function, the lowest cost configuration was rarely in the correct probe shape (3 out of 10), but was 0.5 nm / 20 degree (7 out of 10). However, the structure-RMSD of the lowest cost configuration searched with a different probe shape was comparatively small compared to other cost functions (~1.3 nm). Lastly, when we used the penalty function as the cost function, the result with the smallest probe shape had the lowest cost value. This is reasonable because the penalty function increases its costs if a pixel in a pseudo-AFM image exceeds that of the reference AFM-image, and smaller probe shapes tend to produce images that contain less non-zero pixels because of the small cross section and also make the pixels around the concave regions of molecular surface lower.

Fig 2M-T show the result of the case when the reference-AFM image is generated with the 3 nm radius / 20 degree probe. In this case, the larger tip radius tends to hide fine features on the surface of the specimen, so the structure placement must be more difficult. When we used the cosine similarity as the cost function, the lowest cost configuration was often reached with the correct probe shape (i.e., 3 nm radius / 20 degree)(7 out of 10), but sometimes the 3 nm radius / 10 degree probe had the lowest cost (3 out of 10). The structure-RMSD of those configurations were as small as that in the case of 1nm radius / 20 degree probe (~1.3 nm). When we used the correlation coefficient as the cost function, the results of the correct probe shape often had the lowest cost (7 out of 10) and the structure-RMSD was also low (~1.3 nm). In the case of the pixel-RMSD, the results of the correct probe shape always had the lowest cost and the structure-RMSD was low (~1.3nm). The penalty function favors, as before, the smallest probe.

In summary of the dynein case, the cosine similarity generally worked well and, in the case of relatively blunt probe, the pixel-RMSD and the correlation coefficient worked well, too.

Twin-experiment: Myosin

Next, we conducted otherwise the same examination for a myosin motor domain complex. The myosin motor domain is smaller in size than dynein so that the structure placement is expected to be more difficult than the case of dynein. The results for myosin showed overall the same tendency as the case of dynein (Fig S2). Just in summary, the cosine similarity score worked well both in the structure placement and the probe shape inference in most cases. The correlation coefficient worked well in the structure placement, but it often failed to infer the probe shape. The pixel-RMSD worked better when the reference-AFM image is generated by a larger probe, but otherwise, worked slightly worse. The penalty function always favors smaller probe shape and the structure-RMSD of best-score structure was small.

Twin-experiment: Actin monomer

We further applied the same method to an actin monomer, which is even smaller than the myosin motor domain, and thus is a harder target.

Fig 3E-L show the result when the reference-AFM image is generated by the 1 nm / 10 degree probe. When the cosine similarity is used as the cost function, it had less probability to infer the correct probe shape (4 out of 10) and it was difficult to distinguish the correct one from similar probes, such as 0.5 nm / 10 degree (5 out of 10). The placed structure sometimes had markedly large structure-RMSDs, such as 3 nm, where the orientation was almost opposite. We note that the actin monomer is only weakly anisotropic so that it is rather difficult to distinguish the correct orientation from the opposite one. The prediction by the correlation coefficient showed nearly the same tendency as the cosine similarity. When we used the pixel-RMSD as the cost function, the reconstructed probe shape is rather different from the correct one, but, to our surprise, the placed structure always had relatively small structure-RMSDs. The penalty function showed the same severe artefact as the cases of dynein and myosin.

Fig 3. Twin-experiments for an actin monomer. (A) One of the reference images in the twin-experiment, generated with the 1 nm / 10 degree probe. (B) The image generated from the predicted structure with the cosine similarity-based cost function. (C) One of the reference images in the twin-experiment with the 3 nm / 20 degree probe. (D) The image generated from the predicted structure with the cosine similarity-based cost function. The color bar shows the height in nm (shared by all of the images here). (E-L) The results of twin-experiment with a reference image generated by the 1 nm / 10 degree probe. The row corresponds to the cost function. The leftmost 4 panels (E, G, I, K) show the lowest scores of images. The next 4 panels (F, H, J, L) show the structure-RMSD of the structures with the lowest score. Red vertical dashed lines show the ground-truth probe shape. (M-T) The results of twin-experiment with the reference image generated by the 3 nm / 20 degree probe, shown in the same way as E-L. The cyan vertical dashed lines show the ground-truth probe shape.

Fig 3M-T show the result when the reference AFM image is generated by the 3 nm / 20 degree probe. Using the cosine similarity, it could not infer the probe shape. The structure-RMSD of the best fit configuration sometimes had a large value. The correlation coefficient showed almost the same as the case of the cosine similarity. However, when the pixel-RMSD was used as the cost function, the reconstructed configuration always had relatively small structure-RMSD. The penalty function favors too small probe, as before. All the cost functions did not distinguish the tip apex angle when the probe radius exceeds 3 nm. This is because the highest pixel in the pseudo-AFM image has only 4 nm, thus the conical part of the tip almost never interacts with the protein when the probe radius is larger than 3 nm and the resulting pseudo-AFM image becomes the same.

From those results, when the target protein is relatively small and the target image has pseudo-symmetry, we found that the pixel-RMSD works better than the cosine similarity in terms of the prediction of the placement. When the probe shape is acute, the pixel-RMSD could infer the probe shape, but the accuracy decreases. So, in this case, it could be better to use the pixel-RMSD to find the best configuration and later compare the probe shape by using the cosine similarity. Note that, the pixel-RMSD highly depends

on the absolute value of the heights. Thus, when applying the pixel-RMSD to the experimental data, we need to estimate the stage position in Z direction accurately.

Twin-experiment: Actin filament

As the final case of twin-experiments, we examined a case where we fit a partial molecular structure into a reference AFM image that contains a larger molecular complex. We generated a reference AFM image using 29-mer structure of actin filament (the AFM image in Fig 4AC), which serves as the ground-truth. Note that the actin filament has the directionality; the one end is called the barbed (+) end, and the other called the pointed (-) end. We then used a 15-mer of actin as the structure to be fitted (Fig 4BD). To calculate the structure-RMSD between the predicted structure and the ground-truth structure, we calculated the structure-RMSD between all possible consecutive 15-mer in the reference 29-mer structure and took the minimum value as the structure-RMSD between the prediction and the ground-truth structures.

Fig 4. Twin-experiment for actin filament. (A) One of the reference images used in this twin experiment, generated by a 3 nm / 20 degree probe, with the pixel width 1 nm. (B) The image generated using the structure predicted from the image (A) with the cosine similarity-based cost function. (C) One of the reference images used in this twin experiment, generated by a 3 nm / 20 degree probe. Unlike the panel (A), the pixel width is 2 nm, which is twice as large as that of panel (A). (D) The image generated from the structure predicted from the image (C) with the cosine similarity-based cost function. (E) The resulting best scores of the prediction from the image with 1 nm pixel. The cyan line shows the ground-truth probe shape. (F) The structure-RMSD between the ground-truth structure and the predicted structure from the image with 1nm pixel. (G) The resulting best scores of the prediction from the image with 2 nm-wide pixels. The cyan line shows the ground-truth probe shape. (F) The structure-RMSD between the ground-truth structure and the predicted structure from the image with 2 nm-wide pixels.

First, same as before, we set the pixel/grid size to 1 nm and performed the twin-experiment using the cosine similarity with the same set of probe shapes. The method found the correct probe shape as the lowest cost (8 out of 10) and the structure-RMSD was well small in those configurations (Fig 4EF). Fig S3 shows the result with the other three cost functions. Except the penalty function, other cost functions also found the correct probe shape and the configuration rather accurately. From those results, both the probe shape and configuration can be estimated by using a portion of the complex structure.

Second, we performed the same twin experiment with the image resolution as the pixel/grid size as 2 nm (Fig 4GH), which is twice as large as the previous case. Using the cosine similarity, the probe shape can often be estimated correctly (6 out of 10), or close to the correct shape (3 nm radius /10 degree) otherwise. The best-fit placements had small structure-RMSDs except for one case. For the one failed case, the location of the structure was fine, but the directionality of actin filament was opposite. This failure suggests that, in

case of near-symmetric target molecules, with a low resolution of AFM image (2 nm pixel), the robust inference is difficult.

Fig S3 shows the result with the other cost functions. Using the correlation function, the estimated probe shape has incorrect apex angle, but the probe radius and the configuration were correct. With the pixel-RMSD, it sometimes finds the correct probe shape (4 out of 10), but the majority has incorrect apex angle of 10 degree (6 out of 10). Also, the best-fit structures included filaments of the opposite direction.

From those results, we found that the cosine similarity, the correlation coefficient, and the pixel-RMSD work well for both the probe shape inference and the structure placement when we have an image with 1 nm resolution. However, we also show that when we have an image with the coarser 2 nm resolution, the cosine similarity and the pixel-RMSD worked modestly good and the other cost functions failed to estimate the apex angle of the probe.

Real-data: Actin filament

So far, we applied the exhaustive search rigid-body fitting method to the synthetic-AFM images, i.e., the twin-experiments because we need the ground-truth structure for assessing the accuracy of the predictions. Now, we apply our method to real experimental AFM images. Here we used an HS-AFM image of the actin filament on which we fit the 15-mer structure of actin filament.

First, before the application, we estimated the tilt angle of the stage. The stage surface is close to, but, inevitably, not perfectly parallel to, the *XY*-plane of the AFM apparatus. Thus, the measured Z-coordinate does not directly represent the height of the specimen. For accurate modeling, we first estimated the stage surface and corrected the measured data. To estimate the stage position from the experimental image (Fig 5A), we extracted pixels that are supposed to represent the stage and fitted these pixels by the plane surface via the least square method (Fig 5B). The obtained equation of the surface plane was $z = 0.004x - 0.003y - 18.8\ (nm)$. The surface is indeed close to, but not identical to the *XY*-plane; it has almost 1 nm difference between the edge of the image (Fig S4). We used this equation and subtracted the height of the stage from the apparent data (Fig 5C) at each pixel and chose 40x40 pixels region as a reference AFM image from the corrected image (Fig 5D).

Fig 5. Exhaustive search rigid body fitting to an experimental HS-AFM image of actin filament. (A) The AFM image used in this estimation. (B) The stage position estimated from the background regions of experimental AFM image. (C) The AFM image after the correction of stage position. (D) The reference image used in the rigid-body fitting. It is taken from the lower left rectangular region of the image in C. (E) The pseudo-AFM image generated by the best estimation with the cosine similarity score, with the 3 nm / 10 degree probe that shows the best score. (F) The resulting actin filament structure model on top of the reference AFM image. In (E) and (F), the orientation of the generated actin filament model is indicated by (+) and (-) labels. (G) The lowest cost results using cosine similarity-based cost function. (H) The lowest cost results using pixel-RMSD. (I, J) The results of finer-grid search for shape of the probe using the cosine similarity score (I) and the pixel-RMSD score (J).

Fig 5EF show the result of the exhaustive search rigid-body fitting with the cosine similarity. The probe shape that achieves the lowest cost was 3.0 nm / 10 degree, but the 2.0 nm / 10 degree probe showed a similar result (Fig 5G). Therefore, the actual probe shape seems to be in this range. The result of pixel-RMSD was consistent with these values (Fig 5H). This value is in the range of the typical HS-AFM probe radius 0.5 nm ~ 5.0 nm in literature(8). Then, we further searched the probe shape at a finer grid between 2 nm and 3 nm with 10 and 5 degrees (Fig 5IJ). Both the cosine similarity and the pixel RMSD gave the best score with the probe 2.4 nm / 5 degree (With the apex angle 10 degree, the best estimate of the radius was 2.7 nm). This apex angle of 5 degree suggests that the tip shape is very sharp. This extremely sharp tip shape might suggest the possibility of more complicated rugged shape of the tip or the difference between the pseudo-AFM image generation procedure and the real observation which could distort the results of probe shape estimation.

Finally, we address the inference/prediction of the orientation of the actin filament in the AFM image. We first note that, we cannot identify the orientation of the filament by eye. In the previous section, the twin-experiment showed that our method can identify the orientation accurately for a high-resolution image, but it might fail for a low-resolution image. Then, what about the case of a real AFM image? In the top 10 alignment with the 2.4 nm / 5 degree probe, we found the top 3 structures having the barbed (+) end points at the right, which are followed by the 3 models of the opposite orientation. The 6 out of top 10 structures were in the same direction as the top one. The pixel-RMSD function showed nearly the same results (6 out of top 10 in the same orientation as above). We consider that the grid size, 10 degree, in the search together with the long filament shape limits the number of good/fair fits in each orientation, which may cause the mixture of both orientations. To this end, we repeated otherwise the same exhaustive search with two finer orientation grids, 7.5 and 5.0 degrees. In both cases, all the top 5 structures pointed the barbed (+) end at the right. Out of the top 10, the same orientation appeared in 8 and 7 models for 7.5 and 5.0 degree grids, respectively. We note that, in all the cases when the filament pointed the barbed end at the right, the structure is placed at the edge of the filament of the AFM image. Thus, the presence of the edge in the image could help identifying the orientation. In summary, the orientation of the actin filament is likely to be identified by the exhaustive-search rigid-body fitting, even when it is hardly recognized by visual inspection.

Real-data: $FlhA_C$ ring

Lastly, we applied the exhaustive search rigid-body fitting to the ring-like $FlhA_C$ homo oligomer(32) (Fig 6A). To estimate the stage position, we first extracted regions that are supposed to represent the stage. We performed the least square fitting to the equation of a plane (Fig 6B), and subtracted the height of the stage (Fig 6C). As a target image, we then selected a complex that does not seem to form a complete ring shape as the reference AFM image (Fig 6D). We used 3-, 4-, 5-, 6-, and 7-mer complexes for rigid-body fitting with the cosine similarity as the cost function, finding that the result of 4-mer complex had the lowest cost (Fig 6EF). The 5-mer model was nearly equally good. With that configuration, we inferred the shape of the probe being 2 nm / 5 degree. Fig 6GH shows the result of 4- and 5-mer complex. In both fits, the result with 2 nm /

5 degree has the lowest cost. Thus, we conclude that the probe used to take this AFM image has around 2 nm of the tip radius and 5 degree or less half-apex angle. Since the AFM image seems not to be the complete ring like shape, there could be another monomer that has been detached from the complex we focused on, or some of the monomers might change their conformations. In this case, the obtained 4-mer configuration could differ from the whole complex, but may only represent the part that is intact. For a perturbed part, we can further apply other techniques, such as flexible fitting, using the probe shape information inferred here.

Fig 6. Exhaustive search rigid body fitting to an HS-AFM experimental image of $FlhA_C$ rings/oligomers(32). (A) The AFM image used in this estimation. (B) The stage position estimated from the background regions of experimental AFM image. (C) The AFM image after the correction of stage position. (D) The reference image used in the rigid-body fitting. It is taken from the lower left rectangular region of the image in C. (E) The pseudo-AFM image generated by the estimation result. (F) The resulting FlhAc tetramer structure model on top of the reference AFM image. (G) The lowest cost results using a tetramer model. (H) The lowest cost results using a pentamer model.

Discussion

In this work, we developed the exhaustive search rigid-body fitting method to infer the placement and the probe tip shape that generate most similar pseudo-AFM image to the experimental/reference AFM image. Although there are some limitations, by applying the method with varying probe shape parameters, we showed that the shape of the probe used in the reference AFM image can be inferred. By comparing four score functions, we concluded that the cosine similarity generally works well and, in some difficult cases, the pixel-RMSD may work better than the cosine similarity. We also applied the rigid-body fitting to the two real HS-AFM images, the actin filament and the $FlhA_C$ oligomer, and estimated the shapes of the probes. Since the shape of the probe strongly affects the HS-AFM image, the probe shape will be very important information for further refinement analysis, such as the flexible fitting.

By comparing the four score functions via twin experiments of the grid search method, we concluded that the cosine similarity works well under most of the conditions, both in the probe size estimation and the configuration estimation. The cosine similarity is a function that resembles to the correlation function and has been extensively used in cryo-EM flexible fitting to compare the electron density map(24) and also in the AFM flexible fitting to compare the reference AFM images(23). In the case of small proteins, the pixel-RMSD can work better than the cosine similarity in terms of the placement inference. Therefore, if the results of the cosine similarity have several distinct configurations for small target molecules, it is better to try the pixel-RMSD after fixing the probe geometry by using the cosine similarity score. It should, however, be noted that the pixel-RMSD requires accurate estimation of the stage position.

In fact, these two best scores, the cosine similarity and the pixel-RMSD, are closely related mathematically. To understand the relation, we introduce the pixel heights of both reference and pseudo-AFM images normalized to unity, $H^{(ref)}_{normalized}$ and $H^{(sim)}_{normalized}$ respectively. Then, the pixel-RMSD and the cosine similarity are related by

$$V_{pixel-RMSD}\left(H^{(sim)}_{normalized}; H^{(ref)}_{normalized}\right)^2 = \frac{2}{N} V_{c.s.}\left(H^{(\mathrm{sim})}; H^{(ref)}\right).$$

Namely, the score for the cosine similarity of the original (*unnormalized)* images is proportional to the square of the pixel-RMSD of the *normalized* images. Therefore, only the presence or absence of the normalization is the source of the difference between the two scores. Generally, two images generated with two different probe radii have noticeably different heights only at clefts and cavities on the molecular surface, and the edges of the molecule. This results in relatively small pixel-RMSD values of *unnormalized* images with different probe radii. On the other hand, the sum of the squared heights, which appeared in the normalization factor, depends on the probe radius; it is larger with a larger probe radius. Thus, when the pixel heights of the two images are normalized with different probe radii, the heights would differ at all the pixels, due to the different normalization factor, resulting in a larger pixel-RMSD of the *normalized* images, i.e., the score for the cosine similarity. This property may increase the pixel-RMSD of *normalized* images with different probe radii and contribute to the improved ability of the cosine similarity to detect the difference in probe radii.

We found that the penalty-based cost function is not applicable to the probe size estimation because it always favors smaller probe that produces smaller image. This is because if there are less non-zero pixels in the model AFM image, the opportunity to have a penalty decreases. Because of this feature, sometimes it fails to estimate the configuration. We note that, this penalty-based function is not the same as that used in the previous research. The penalty-based cost function used in this work calculates cost using the height of pixels in an AFM image, and the previous research calculates the cost using coordinates of particles.

In both of two experimental AFM images, the estimated probe angle was extremely sharp (5 degree or less), compared to the value guessed in other researches(21,22), which were around 20 degree. It is possible that the apex-angle differs largely sample by sample. Alternatively, there could be another possibility that the observation method of HS-AFM, the tapping mode in the HS-AFM, caused this difference. Since, in the tapping mode, the probe always vibrates and only taps the sample and quickly detaches from it, the lateral part of the probe has less chance to collides with the sample. Thus, the resulting image could contain the effect of tapping and the estimated probe shape might be affected by those artifacts. Although the estimated probe shape is possibly affected by the observation technique, the result of estimation can be used as an effective probe shape in the successive analysis, such as flexible fitting, because the systematic error caused by the effective tip radius can be described by the current tip model. To decipher these points, it may be interesting to include the vibrating cantilever and probe tip controlled via a feedback within the molecular simulation systems, although this makes the estimate much more time consuming.

In this paper, for simplicity, we modeled a probe tip as a combination of simple geometric shapes that can be controlled only by two parameters, the hemisphere radius and the half apex angle of a circular frustum of a cone. In reality, however, the probe shape could have much more complicated shape. In theory, since neither the image similarity function form nor pseudo-AFM image generation algorithm depends on the shape of the probe, it is possible to model more complicated probe tip geometry by a polygon mesh or a

set of voxels and optimize the probe shape iteratively, such as Markov chain Monte Carlo simulation in a similar framework. However, practically, since the accuracy of the estimation is bound by the resolution, it would be hard to estimate the shape if the target HS-AFM image does not have the exceptionally high spatial resolution and small level of noises and otherwise it would lead overfitting.

Technically, searching the best location of a molecular model can be speeded up by using the fast Fourier transformation (FFT)(33). However, within our program, we found that the most time-consuming operation was not the translational search, but the pseudo-AFM image generation for all the discrete orientations of molecules. Also, as the FFT imposes periodicity and wraps around the borders of AFM images instead of just cropping, it could lead to incorrect score values when the molecule(s) located at the borders of the image. Therefore, we did not use the FFT-based method here for the translational search. In the AFM image case, the data are two-dimensional images and the grid size (~1nm) is larger than that of the docking simulation (~0.1 nm) where the FFT is of more importance. We have much less grids (typically, the order of 10^3 or 10^4 after focusing on a region of interest) compared to the three-dimensional docking simulation (typically, 10^6 grids).

In our development stage, we tried to use the Monte Carlo simulated annealing for the search process, as in our previous study(23). The Monte Carlo process includes translational and rotational movements of the target molecule, as well as the change in probe tip shape. This stochastic search worked well in some cases when the temperature cooling schedule was fine-tuned. We, however, found that the temperature cooling schedule that works well differs case by case and thus must be carefully tuned for each target system. Often, this tuning was not straightforward. In addition, we need to repeat many independent runs to confirm that we reached the global minimum, without being trapped to a metastable basin. Altogether, we concluded that the simulated annealing is not the best approach for this rigid-body fitting, and decided to employ the exhaustive search protocol, which does not need any simulation parameters to be tuned and is more robust. We anticipate that the cost function landscape does not have a funnel-like shape, but may have a golf-course-like shape, in which the configuration space that has a low-cost function is narrow only around the global minimum. Outside this narrow region, the landscape has some noise-driven ruggedness with no global bias towards the global minimum. In such a case, the stochastic search does not work well, in general.

Acknowledgement

We thank Noriyuki Kodera, and Naoya Terahara and Tohru Minamino for giving the HS-AFM data of actin filament and flagellar $FlhA_C$, respectively. This work was partly supported by the Japan Science and Technology Agency (JST) grant (JPMJCR1762) (S.T. and Y.M.) and JSPS KAKENHI Grant Number 19J14515 (T.N.).

1. Deniz AA, Mukhopadhyay S, Lemke EA. Single-molecule biophysics: At the interface of biology, physics and chemistry. J R Soc Interface. 2008;5(18):15–45.
2. Moerner WE, Fromm DP. Methods of single-molecule fluorescence spectroscopy and microscopy. Rev Sci Instrum. 2003;74(8):3597–619.
3. Mazal H, Haran G. Single-molecule FRET methods to study the dynamics of proteins at work. Curr Opin Biomed Eng [Internet]. 2019;12:8–17. Available from: https://doi.org/10.1016/j.cobme.2019.08.007
4. Bacic L, Sabantsev A, Deindl S. Recent advances in single-molecule fluorescence microscopy render structural biology dynamic. Curr Opin Struct Biol [Internet]. 2020;65:61–8. Available from: https://doi.org/10.1016/j.sbi.2020.05.006
5. Saxton MJ, Jacobson K. Single-particle tracking: Applications to membrane dynamics. Annu Rev Biophys Biomol Struct. 1997;26:373–99.
6. Moffitt JR, Chemla YR, Smith SB, Bustamante C. Recent advances in optical tweezers. Annu Rev Biochem. 2008;77:205–28.
7. Alessandrini A, Facci P. AFM: A versatile tool in biophysics. Meas Sci Technol. 2005;16(6).
8. Ando T, Uchihashi T, Kodera N. High-Speed AFM and Applications to Biomolecular Systems. Annu Rev Biophys [Internet]. 2013;42(1):393–414. Available from: http://www.annualreviews.org/doi/10.1146/annurev-biophys-083012-130324
9. Ando T. High-speed atomic force microscopy and its future prospects. Biophys Rev. 2018;10(2):285–92.
10. Uchihashi T, Iino R, Ando T, Noji H. High-speed atomic force microscopy reveals rotary catalysis of rotorless F 1-ATPase. Science (80-) [Internet]. 2011 Aug 5;333(6043):755–8. Available from: http://www.sciencemag.org/cgi/doi/10.1126/science.1205510
11. Kodera N, Yamamoto D, Ishikawa R, Ando T. Video imaging of walking myosin V by high-speed atomic force microscopy. Nature [Internet]. 2010 Nov 10;468(7320):72–6. Available from: http://dx.doi.org/10.1038/nature09450
12. Shibata M, Yamashita H, Uchihashi T, Kandori H, Ando T. High-speed atomic force microscopy shows dynamic molecular processes in photoactivated bacteriorhodopsin. Nat Nanotechnol [Internet]. 2010;5(3):208–12. Available from: http://dx.doi.org/10.1038/nnano.2010.7
13. Miyagi A, Chipot C, Rangl M, Scheuring S. High-speed atomic force microscopy shows that annexin V stabilizes membranes on the second timescale. Nat Nanotechnol [Internet]. 2016;11(9):783–90. Available from: http://dx.doi.org/10.1038/nnano.2016.89
14. Shibata M, Nishimasu H, Kodera N, Hirano S, Ando T, Uchihashi T, et al. Real-space and real-Time dynamics of CRISPR-Cas9 visualized by high-speed atomic force microscopy. Nat Commun [Internet]. 2017;8(1):1–9. Available from: http://dx.doi.org/10.1038/s41467-017-01466-8
15. Kodera N, Noshiro D, Dora SK, Mori T, Habchi J, Blocquel D, et al. Structural and dynamics analysis of intrinsically disordered proteins by high-speed atomic force microscopy. Nat Nanotechnol [Internet]. 2020; Available from: http://dx.doi.org/10.1038/s41565-020-00798-9

16. Scheuring S, Boudier T, Sturgis JN. From high-resolution AFM topographs to atomic models of supramolecular assemblies. J Struct Biol. 2007;159(2 SPEC. ISS.):268–76.
17. Trinh MH, Odorico M, Pique ME, Teulon JM, Roberts VA, Ten Eyck LF, et al. Computational reconstruction of multidomain proteins using atomic force microscopy data. Structure [Internet]. 2012;20(1):113–20. Available from: http://dx.doi.org/10.1016/j.str.2011.10.023
18. Chaves RC, Pellequer JL, Tramontano A. DockAFM: Benchmarking protein structures by docking under AFM topographs. Bioinformatics. 2013;29(24):3230–1.
19. Chaves RC, Teulon J-M, Odorico M, Parot P, Chen SW, Pellequer J-L. Conformational dynamics of individual antibodies using computational docking and AFM. J Mol Recognit. 2013;26(11):596–604.
20. Dasgupta B, Miyashita O, Tama F. Reconstruction of low-resolution molecular structures from simulated atomic force microscopy images. Biochim Biophys Acta - Gen Subj [Internet]. 2020;1864(2):129420. Available from: https://doi.org/10.1016/j.bbagen.2019.129420
21. Trinh MH, Odorico M, Bellanger L, Jacquemond M, Parot P, Pellequer JL. Tobacco mosaic virus as an AFM tip calibrator. J Mol Recognit. 2011;24(3):503–10.
22. Lutter L, Serpell CJ, Tuite MF, Serpell LC, Xue WF. Three-dimensional reconstruction of individual helical nano-filament structures from atomic force microscopy topographs. Biomol Concepts. 2020;11(1):102–15.
23. Niina T, Fuchigami S, Takada S. Flexible Fitting of Biomolecular Structures to Atomic Force Microscopy Images via Biased Molecular Simulations. J Chem Theory Comput. 2020;16(2):1349–58.
24. Orzechowski M, Tama F. Flexible fitting of high-resolution x-ray structures into cryoelectron microscopy maps using biased molecular dynamics simulations. Biophys J. 2008;95(12):5692–705.
25. Fuchigami S, Niina T, Takada S. Bayesian Statistical Inference of Experimental Parameters via Biomolecular Simulations: Atomic Force Microscopy. Front Mol Biosci. 2021;8:56.
26. Ando T, Kodera N, Uchihashi T, Miyagi A, Nakakita R, Yamashita H, et al. High-speed atomic force microscopy for capturing dynamic behavior of protein molecules at work. e-Journal Surf Sci Nanotechnol. 2005;3(December):384–92.
27. Amyot R, Flechsig H. BioAFMviewer: An interactive interface for simulated AFM scanning of biomolecular structures and dynamics. PLoS Comput Biol [Internet]. 2020;16(11):1–12. Available from: http://dx.doi.org/10.1371/journal.pcbi.1008444
28. Niina T, Kato S, Koide H. ToruNiina/afmize [Internet]. zenodo. zenodo; 2020. Available from: https://github.com/ToruNiina/afmize
29. Kubo S, Li W, Takada S. Allosteric conformational change cascade in cytoplasmic dynein revealed by structure-based molecular simulations. PLoS Comput Biol. 2017;13(9):1–27.
30. Sack S, Müller J, Marx A, Thormählen M, Mandelkow EM, Brady ST, et al. X-ray structure of motor and neck domains from rat brain kinesin. Biochemistry. 1997;36(51):16155–65.
31. Gurel PS, Kim LY, Ruijgrok P V., Omabegho T, Bryant Z, Alushin GM. Cryo-EM structures reveal specialization at the myosin VI-actin interface and a mechanism of force sensitivity. Elife. 2017;6(Md):1–33.

32. Terahara N, Inoue Y, Kodera N, Morimoto VY, Uchihashi T, Imada K, et al. Insight into structural remodeling of the FlhA ring responsible for bacterial flagellar type III protein export. Sci Adv. 2018;4(4):eaao7054.
33. Katchalski-Katzir E, Shariv I, Eisenstein M, Friesem AA, Aflalo C, Vakser IA. Molecular surface recognition: Determination of geometric fit between proteins and their ligands by correlation techniques. Proc Natl Acad Sci U S A. 1992;89(6):2195–9.

Fig S1. Noise distributions in the background regions of experimental AFM images. We used two AFM movies that contains large background regions, $FlhA_C$ monomer (Top) and actin filament (Bottom). After extracting background regions manually, we estimated the stage plane by a simple least squares method and then collected the deviation from the estimated stage height. We took the last 5 frames in the AFM movie. By construction, the mean of the noise is almost equal to zero. The standard deviation of the distribution is 0.284 nm in the case of $FlhA_C$ and 0.347 nm in the case of actin filament.

Fig S2. Twin-experiments for myosin. (A) One of the reference images in the twin-experiment with the 1 nm / 10 degree probe. (B) The image generated from the predicted structure with the cosine similarity-based cost function. (C) One of the reference images in the twin-experiment with the 3 nm / 20 degree probe. (D) The image generated from the predicted structure with the cosine similarity-based cost function. The color bar shows the height in nm (shared by all of the images here). (E-L) The results of twin-experiment with a reference image generated by the 1 nm / 10 degree probe. The row corresponds to the cost function. The leftmost 4 panels (E, G, I, K) show the lowest scores of images. The next 4 panels (F, H, J, L) show the structure-RMSD of the structures with the lowest score. Red vertical dashed lines show the ground-truth probe shape. (M-T) The results of twin-experiment with a reference image generated by the 3 nm / 20 degree probe, shown in the same way as E-L. The cyan vertical dashed lines show the ground-truth probe shape.

Fig S3. Twin-experiments with actin filament. The left 2 columns (ABEFIJ) show the result of the prediction from images with 1nm-wide pixels. The right 2 columns (CDGHKL) show the result with 2nm-wide pixels. The top row (A-D) shows the results with the correlation-based cost function. The middle row (E-H) shows the results with the pixel-RMSD. The bottom row (I-L) shows the results with the penalty function.

Fig S4. **The stage position is estimated by a simple least square method.** The left panel shows the experimental image of actin filament. The right panel shows the actual data (gray line) and the estimated position of the stage (red line) along the white dotted line in the left panel.

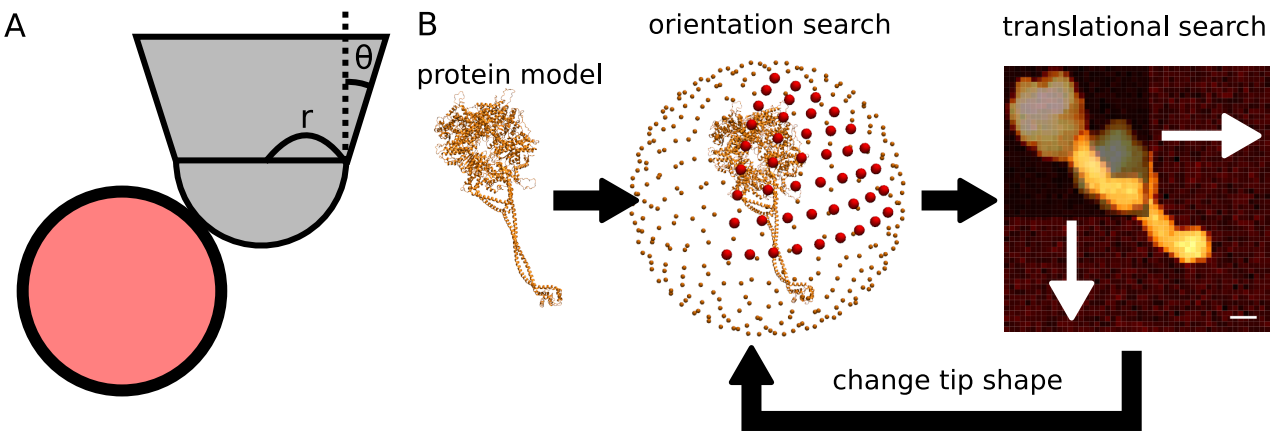
A
θ
r
B
protein model
orientation search
translational search
change tip shape

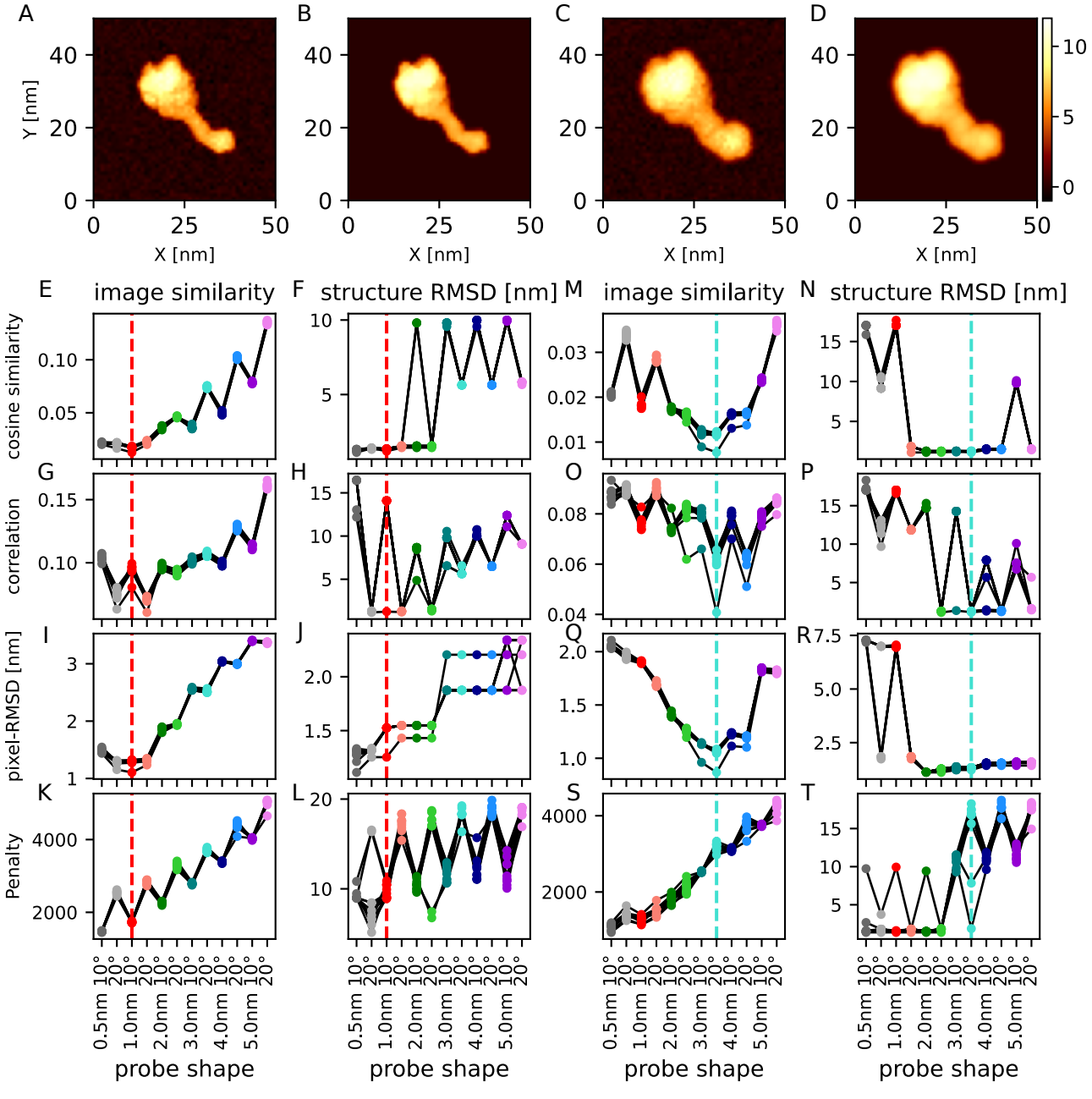
A
B
C
D
Y [nm]
X [nm]
E
image similarity
F
structure RMSD [nm]
M
image similarity
N
structure RMSD [nm]
cosine similarity
G
H
O
P
correlation
I
J
Q
R
pixel-RMSD [nm]
K
L
S
T
Penalty
0.5nm 10° 20°
1.0nm 10° 20°
2.0nm 10° 20°
3.0nm 10° 20°
4.0nm 10° 20°
5.0nm 10° 20°
probe shape

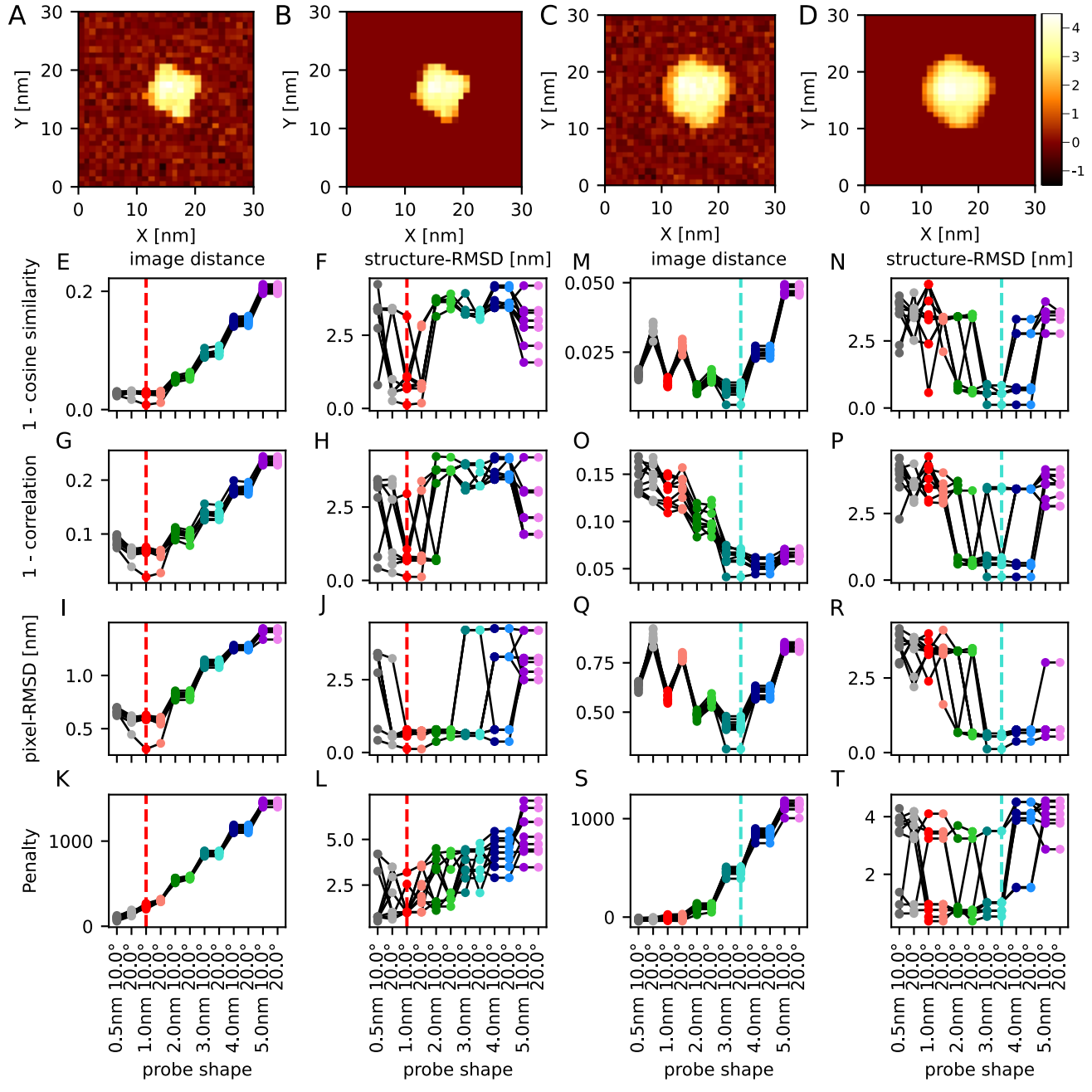
A
B
C
D
Y [nm]
X [nm]
image distance
structure-RMSD [nm]
1 - cosine similarity
1 - correlation
pixel-RMSD [nm]
Penalty
probe shape
0.5nm 10.0°
1.0nm 10.0°
2.0nm 10.0°
3.0nm 10.0°
4.0nm 10.0°
5.0nm 10.0°
0.5nm 20.0°
1.0nm 20.0°
2.0nm 20.0°
3.0nm 20.0°
4.0nm 20.0°
5.0nm 20.0°

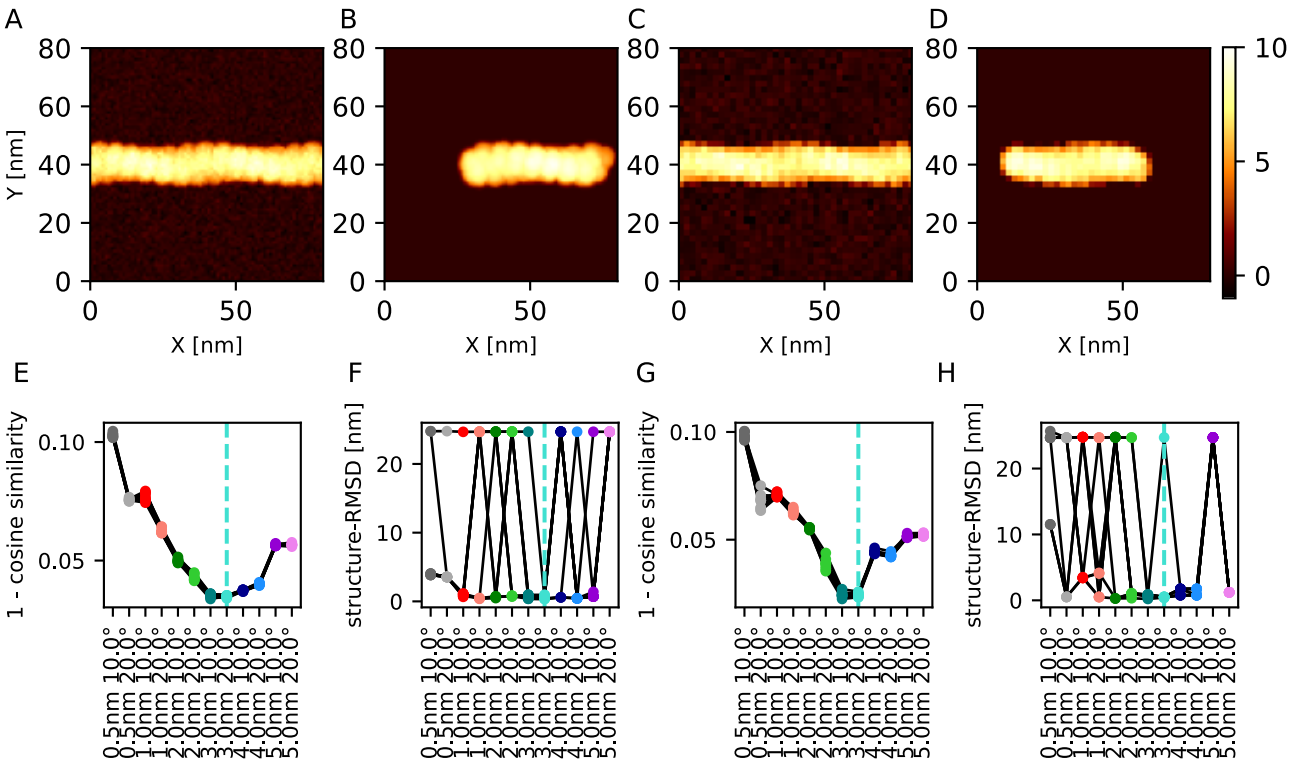
A
B
C
D
Y [nm]
X [nm]
0
20
40
60
80
50
10
5
E
F
G
H
1 - cosine similarity
structure-RMSD [nm]
0.10
0.05
0.5nm 10.0°
0.5nm 20.0°
1.0nm 10.0°
1.0nm 20.0°
2.0nm 10.0°
2.0nm 20.0°
3.0nm 10.0°
3.0nm 20.0°
4.0nm 10.0°
4.0nm 20.0°
5.0nm 10.0°
5.0nm 20.0°

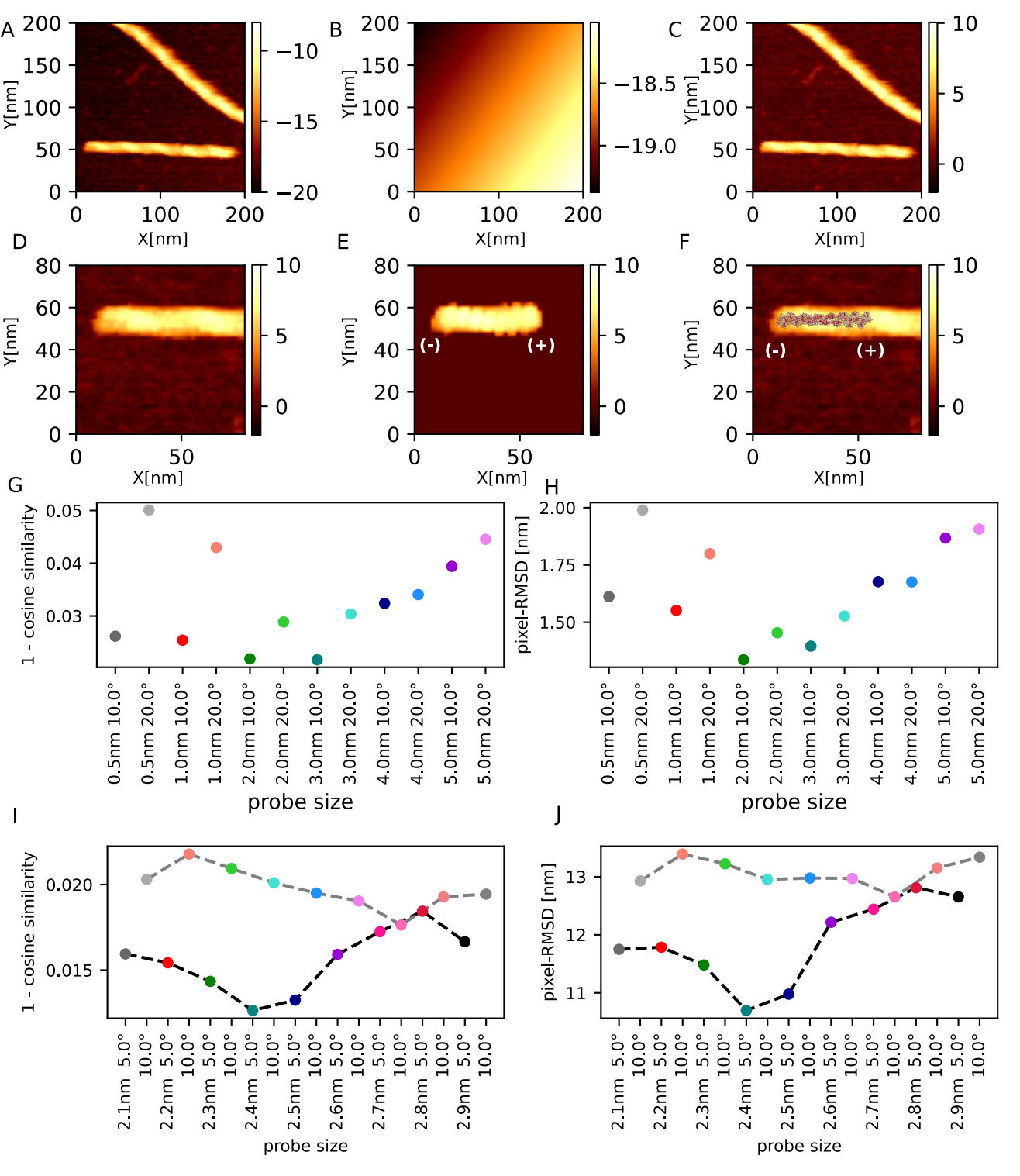
A
B
C
D
E
F
G
H
I
J
Y[nm]
X[nm]
(-)
(+)
1 - cosine similarity
pixel-RMSD [nm]
probe size
0.5nm 10.0°
0.5nm 20.0°
1.0nm 10.0°
1.0nm 20.0°
2.0nm 10.0°
2.0nm 20.0°
3.0nm 10.0°
3.0nm 20.0°
4.0nm 10.0°
4.0nm 20.0°
5.0nm 10.0°
5.0nm 20.0°
2.1nm 5.0°
2.1nm 10.0°
2.2nm 5.0°
2.2nm 10.0°
2.3nm 5.0°
2.3nm 10.0°
2.4nm 5.0°
2.4nm 10.0°
2.5nm 5.0°
2.5nm 10.0°
2.6nm 5.0°
2.6nm 10.0°
2.7nm 5.0°
2.7nm 10.0°
2.8nm 5.0°
2.8nm 10.0°
2.9nm 5.0°
2.9nm 10.0°

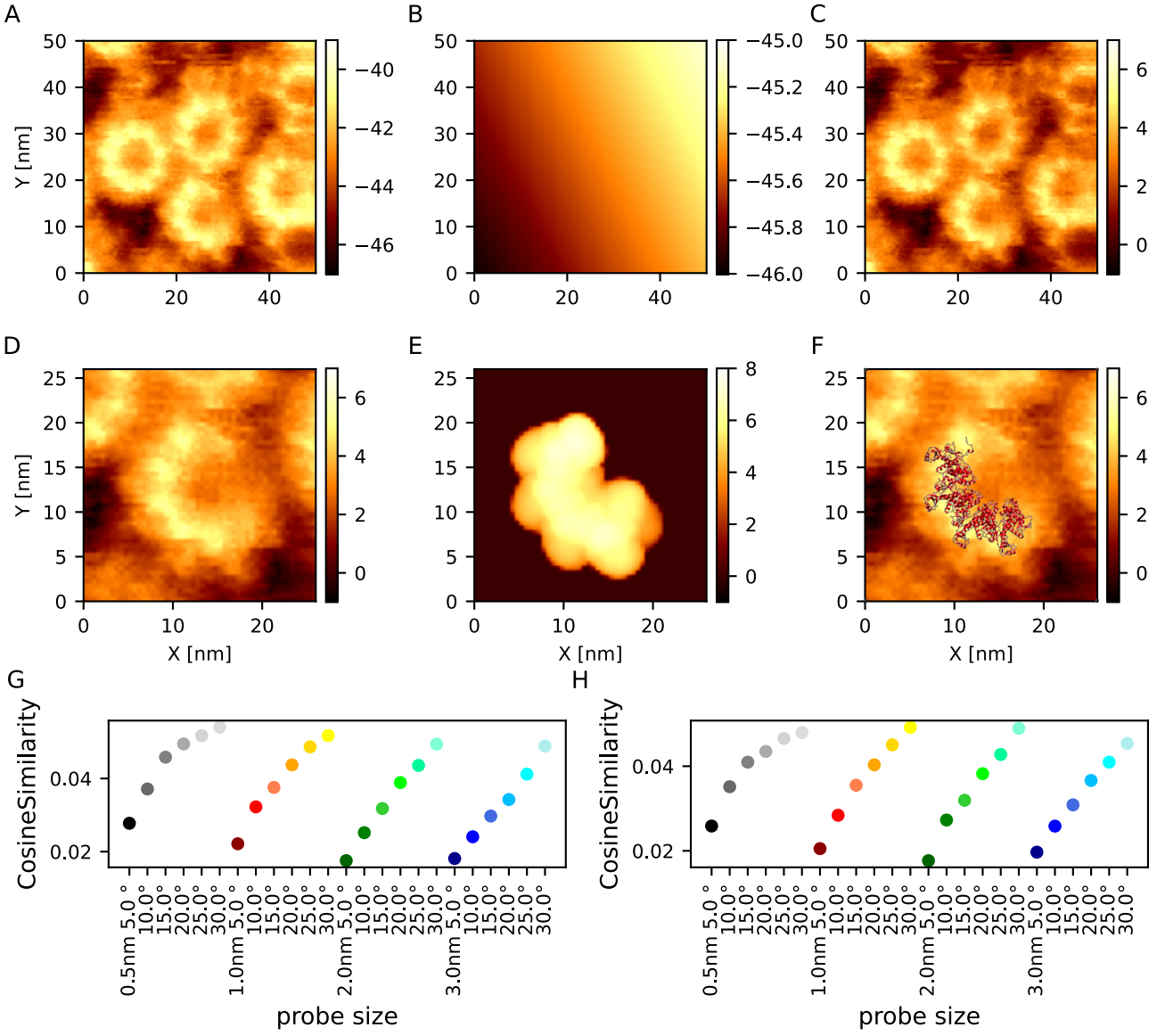
A
B
C
D
E
F
G
H
Y [nm]
X [nm]
CosineSimilarity
probe size
0.5nm 5.0 °
10.0 °
15.0 °
20.0 °
25.0 °
30.0 °
1.0nm 5.0 °
2.0nm 5.0 °
3.0nm 5.0 °

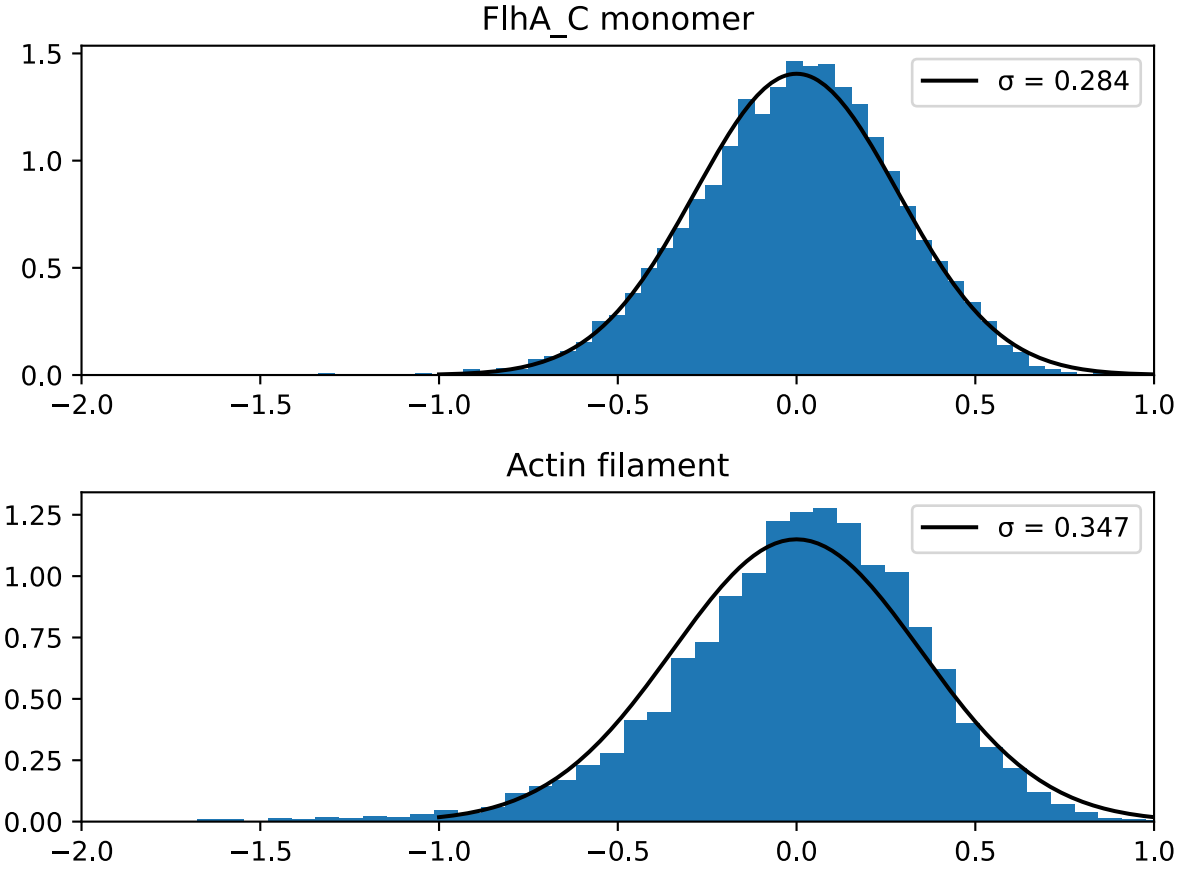
FlhA_C monomer
σ = 0.284
1.5
1.0
0.5
0.0
−2.0
−1.5
−1.0
−0.5
0.0
0.5
1.0
Actin filament
σ = 0.347
1.25
1.00
0.75
0.50
0.25
0.00
−2.0
−1.5
−1.0
−0.5
0.0
0.5
1.0

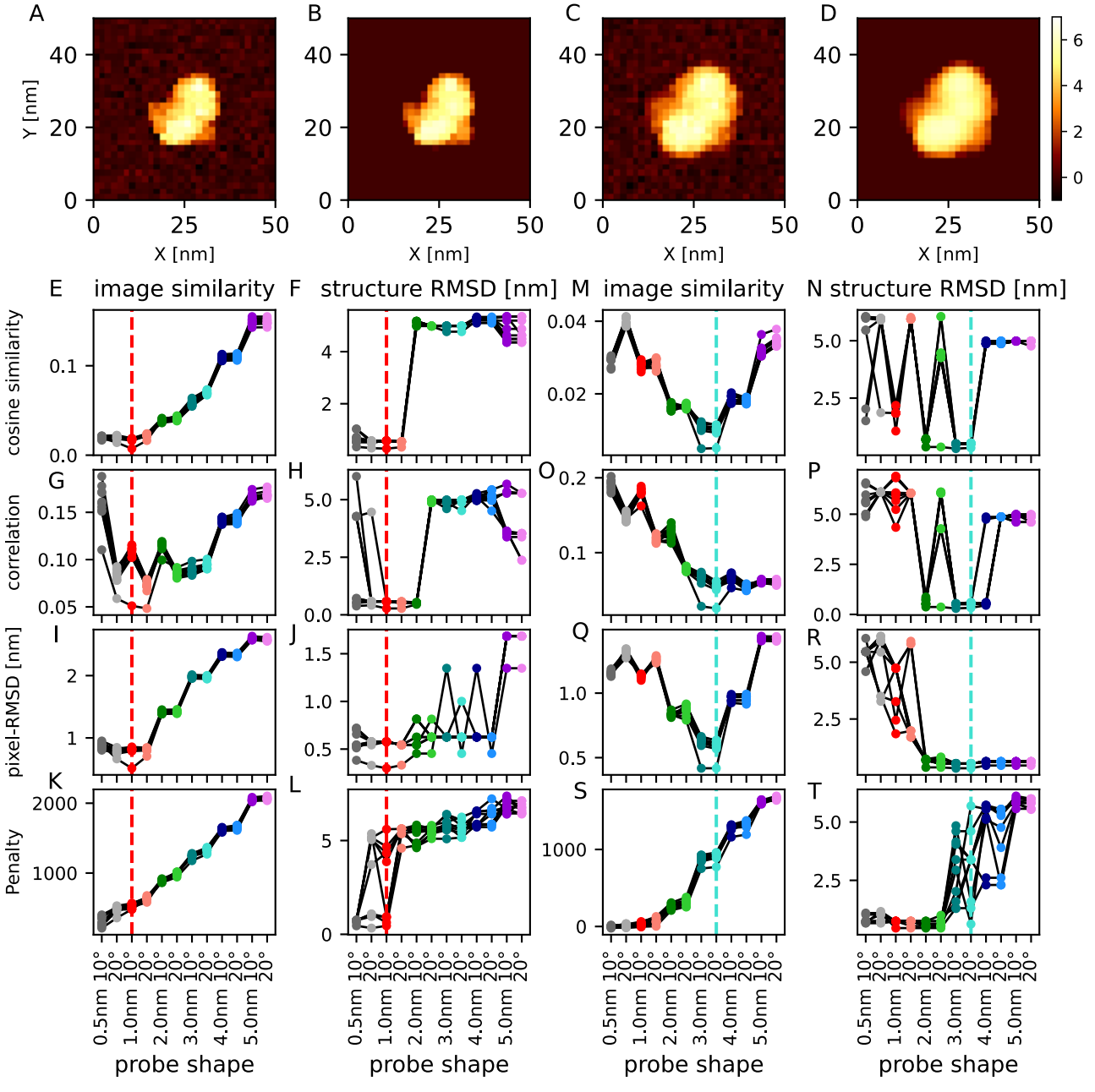
A
B
C
D
Y [nm]
X [nm]
E image similarity
F structure RMSD [nm]
M image similarity
N structure RMSD [nm]
cosine similarity
correlation
pixel-RMSD [nm]
Penalty
probe shape
0.5nm 10° 20°
1.0nm 10° 20°
2.0nm 10° 20°
3.0nm 10° 20°
4.0nm 10° 20°
5.0nm 10° 20°

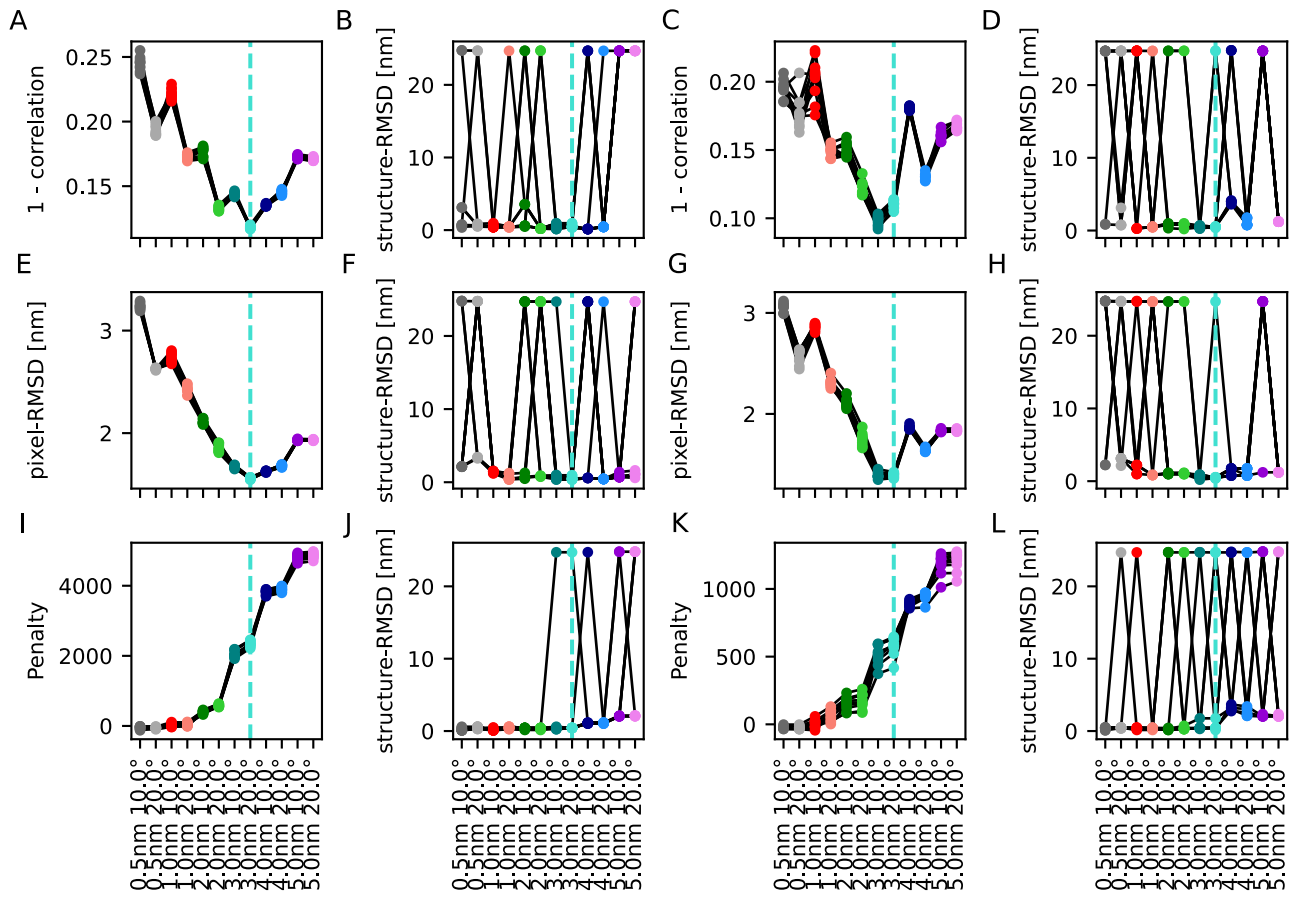
A
B
C
D
E
F
G
H
I
J
K
L
1 - correlation
pixel-RMSD [nm]
Penalty
structure-RMSD [nm]
0.5nm 10.0°
0.5nm 20.0°
1.0nm 10.0°
1.0nm 20.0°
2.0nm 10.0°
2.0nm 20.0°
3.0nm 10.0°
3.0nm 20.0°
4.0nm 10.0°
4.0nm 20.0°
5.0nm 10.0°
5.0nm 20.0°

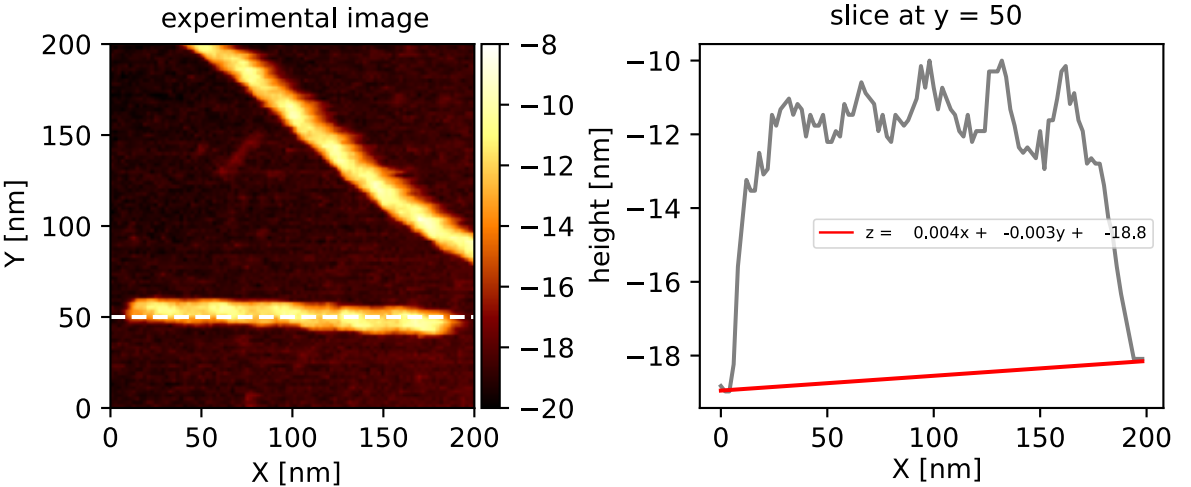
experimental image
Y [nm]
X [nm]
200
150
100
50
0
0
50
100
150
200
−8
−10
−12
−14
−16
−18
−20
slice at y = 50
height [nm]
X [nm]
−10
−12
−14
−16
−18
0
50
100
150
200
z = 0.004x + -0.003y + -18.8